Granular flow in a Rotating Drum

Gregory L. Wagner

December 19, 2013

1 Introduction

Granular materials are encountered regularly in everyday life — as salt and sugar in the kitchen, as dirt on a trail underfoot, or as sand on the beach. They are agents in destructive and powerful events: vast avalanches of snow and ice, pyroclastic flows of hot dust and gas down the flanks of an erupting volcano, and landslides and mass wasting on Earth and other rocky bodies of the solar system. In human industries like the food, pharmaceutical, and semiconductor industry, granular materials are the second most manipulated substance after water [13].

An understanding of the mechanics of granular flows is necessary to interpret and predict their behavior in geophysical and industrial contexts. In general, granular flows can be divided into three regimes depending on their rate of deformation: a dense, quasi-static regime, a slowly flowing "liquid" regime, and a relatively dilute, rapidly flowing "gaseous" regime. The quasi-static regime is characterized by slow deformation and frictional interaction between particles and is well-studied in the field of soil mechanics [14]. The gaseous regime is characterized by binary collisions and can be described by a kinetic theory which accounts for dissipation in collisions [6]. The liquid regime, which is the subject of this work, is characterized both by collisions and enduring contacts and presents perhaps the greatest theoretical challenge [5].

A theoretical description of the liquid regime of granular flow based on the microscopic physics of particle interactions has proven elusive. However, empirical laws proposed relatively recently which employ the principles of mass and momentum conservation in a continuum approximation – a "hydrodynamic description" – have demonstrated some success [9, 5]. This approach decomposes the bulk stress in the granular medium into a "pressure" (often taken to be isotropic) and a deviatoric component. For the deviatoric component a "frictional" rheological law is proposed which is proportional to the pressure and coaxial with the rate of strain. In addition, the coefficient of proportionality or friction coefficient μ has a functional dependence on the "inertia number" I which is dependent on magnitude of the rate of strain, particle diameter, pressure, and bulk density of the material. We call this empirical rheology the "$\mu(I)$ law".

The $\mu(I)$ law is particularly interesting because, while it uses material parameters and has a dependence on the inertia number which is determined by shear cell and inclined plane experiments, it has provided accurate quantitative predictions for the velocity profile and flowing layer depth in an independent heap flow experiment [9] (for a description of the common experimental configurations used in the study of granular flow see [10]). In this

work, we examine whether the $\mu(I)$ law is valid for a fourth common configuration: the rotating drum.

Granular flows in rotating drums, like flows on a heap, are surface flows in that the flowing grains occupy a layer over a bed surface of static grains. One of the special characteristics of surface flows is that they exhibit two distinct regimes of behavior depending on the flow rate. At low flow rates, the system episodically avalanches: grains either accumulate (heap flow) or rotate as a solid body (rotating drum) until a critical pile inclination is reached at which they release in an avalanche. At high flow rates a continuously flowing layer of grains forms. Flow in a rotating drum is more complicated than flow on a heap because it is not necessarily homogeneous in the direction of flow. Nevertheless the rotating drum configuration uses far less granular material and permits a higher volume of experiments because grains are automatically recycled. Further, the rotating drum can access a greater range of average surface inclinations (although the shape of the surface may not remain flat) [10]. As a result much attention has been devoted to the rotating drum, including investigations into the properties of the continuously flowing layer [7], avalanches [3, 12], the transition between episodic avalanching and continuous flow [1, 4], discrete element method simulations [17, 16], explanations for the shape of the free surface [15], and studies that use experimental techniques such as MRI [16] and positron emission [11].

In this work we conduct a general investigation into the characteristics of flow in a rotating drum with an emphasis on applying the $\mu(I)$ rheology to describe both the continuously flowing layer as well as the episodic avalanches. We develop separate theories for the continuously flowing layer and for the episodic avalanching regime. We compare the predictions of the theory to experiments performed in Vancouver at the University of British Columbia as well as experiments in a second drum in the GFD lab at the Woods Hole Oceanographic Institution. We also comment on the transition from episodic avalanching and continuous flow, although it is not yet completely understood.

This report is organized as follows. In Section 2 we describe our experimental methods and materials. In Section 3 we discuss representative experimental results and introduce the main features of the flow including episodic avalanching, continuous flow, and the transition between these regimes. In addition we present our observations of the effects of drum width and drum radius on the relationship between flow rate and the inclination of grain pile. In Section 4 we give a brief introduction to the theory of the liquid regime of granular flow and the $\mu(I)$ rheology and derive two models: the "thin, shallow, slippy" (or TSS) model for the continuously flowing layer, and a "crude inertial model". In Section 5 we compare the predictions of our theory with experimental observations. We find that the TSS model appears to be valid for thin drums within a certain range of flow rates within the continuously flowing regime. However it does not appear to be valid for the wider drums (as expected), and underpredicts the angle of the flowing layer at both the high and low ends of the tested flow rates. Further we are unable to fully validate the model because it depends on material parameters which have not yet been measured. For the crude inertial model we only attempt a qualitative comparison. We find that it can produce a flow which resembles an avalanche and provides some basis for an explanation for why the system might transition from episodic avalanching to continuous flow as the flow rate is increased (but not the converse transition from continuous flow to episodic avalanching).

2 Experimental method and materials

Results are presented for experiments conducted in the GFD lab at the Woods Hole Oceanographic Institution in Woods Hole, Massachusetts during the Program in Geophysical Fluid Dynamics in the summer of 2013, as well as for experiments conducted earlier at the University of British Columbia in Vancouver, British Columbia.

2.1 Apparati

Two different drums were used for experiments: one (Vancouver) with radius 144 mm located at the University of British Columbia in Vancouver, and another (Woods Hole) with radius 69 mm located in the GFD Lab at the Woods Hole Oceanographic Institution in Woods Hole, Massachusetts. An image of each is shown in Figure 1(A) and 1(B). The exterior of both drums was composed of Perspex. The width of the Vancouver drum could be varied by fixing a Perspex plate at the desired position. The width of the Woods Hole drum was varied by inserting a circular piece of rigid, high density foam with a slightly smaller diameter than the drum. The foam was stacked on top of sheets of additional foam and Perspex against the back wall of the drum to achieve the desired width.

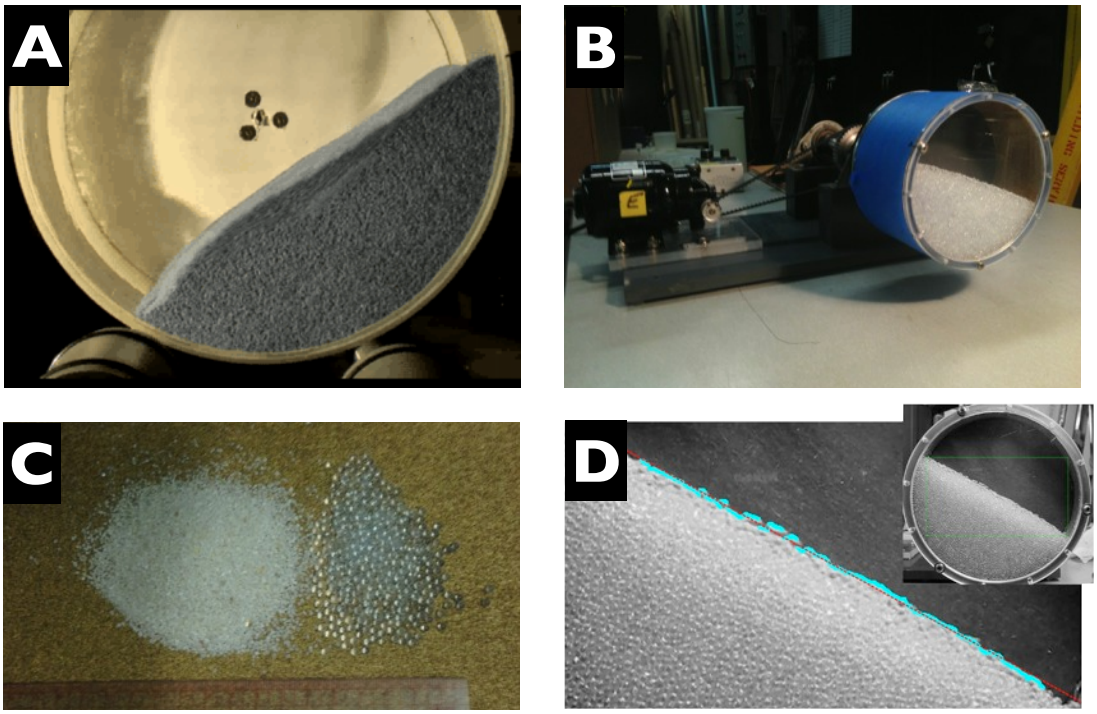

Figure 1: Experimental apparati, materials, and procedure for measuring the surface inclination. (A) Vancouver drum with radius 144 mm; (B) the entire Woods Hole set-up including the motor driving drum rotation. The Woods Hole drum has radius 69 mm and here is filled with Ballotini spherical glass beads of diameter 2 mm, (C) decorative aquarium sand (left) and 3mm spherical class beads (right), (D) illustration of the image cropping and line fitting procedure to determine the pile angle θ.

2.2 Materials

We performed experiments with four granular media: "Ballotini" spherical glass beads of diameter 1.5, 2, and 3 mm, and decorative aquarium sand of irregular shape and characteristic diameter ≈ 1 mm. An image of the decorative aquarium sand and 3mm spherical glass beads is shown in Figure 1(C).

2.3 Method

The experimental protocol for each drum was slightly different. The Vancouver drum was computer-controlled with an automated system for imaging the drum from the side and calculating the slope angle instantaneously so that many thousands of images did not have to be saved. The Woods Hole drum was controlled manually and video was taken by a camera on a tripod and analyzed later.

Because it was possible to automate the collection of large amounts of data in the Vancouver drum, very long "burn" runs were performed in which the glass beads were rotated for periods of up to 8–12 hours. From these runs it appears that the inclination of the pile does undergo a slow drift over extended runs, perhaps due to wearing of the beads and the associated accumulation of glass powder or dust. Further, if the beads were removed from the drum after a burn, washed to remove dust, and reinserted, a sudden change in the measured slopes was observed. This change in measured slope after washing would then be followed by a *second* slow drift in slope inclination before reaching a steady-state. A full characterization of the wearing properties and the apparent effect of accumulated dust is beyond the scope of this work. It is important to note, however, that all results presented for the Vancouver drum have undergone this "burning" process, whereas in the Woods Hole drum such a procedure would not have been practical.

For the Woods Hole drum, the rotation speed was set by a manual controller which was characterized to relate the scale of the controller to the rotation speed of the drum. The protocol involved starting the drum at the maximum rotation speed allowable by the controller. The rotation speed was then decreased in small increments until the minimum rotation speed for which the motor could drive the drum steadily (lower rotation speeds were possible, but "skipping" and irregular movements of the motor were observed), and then increased in small increments until the maximum rotation speed was again reached. This allowed the transition between continuous flow and episodic avalanching to be explored taking into account any potential hysteretic effects due to the history and past states of the system. For each rotation speed a short video approximately 2 minutes long was recorded for analysis.

To determine the average angle of the flowing layer from the video, a portion of each video frame containing only the layer of beads and the dark drum background was extracted. The surface of the grain pile was located according to an increase in grayscale intensity above some threshold. A line was then fit to these points from which the angle of the layer was calculated. An image of showing the cropped area of the drum image and a line fit to the layer surface is shown in Figure 1(D).

3 Experimental Results

3.1 Two regimes of flow

Figure 2 shows some representative time traces of the pile angle θ versus time for various rotation rates Ω taken from the Vancouver experiments with 2 mm glass beads. From the

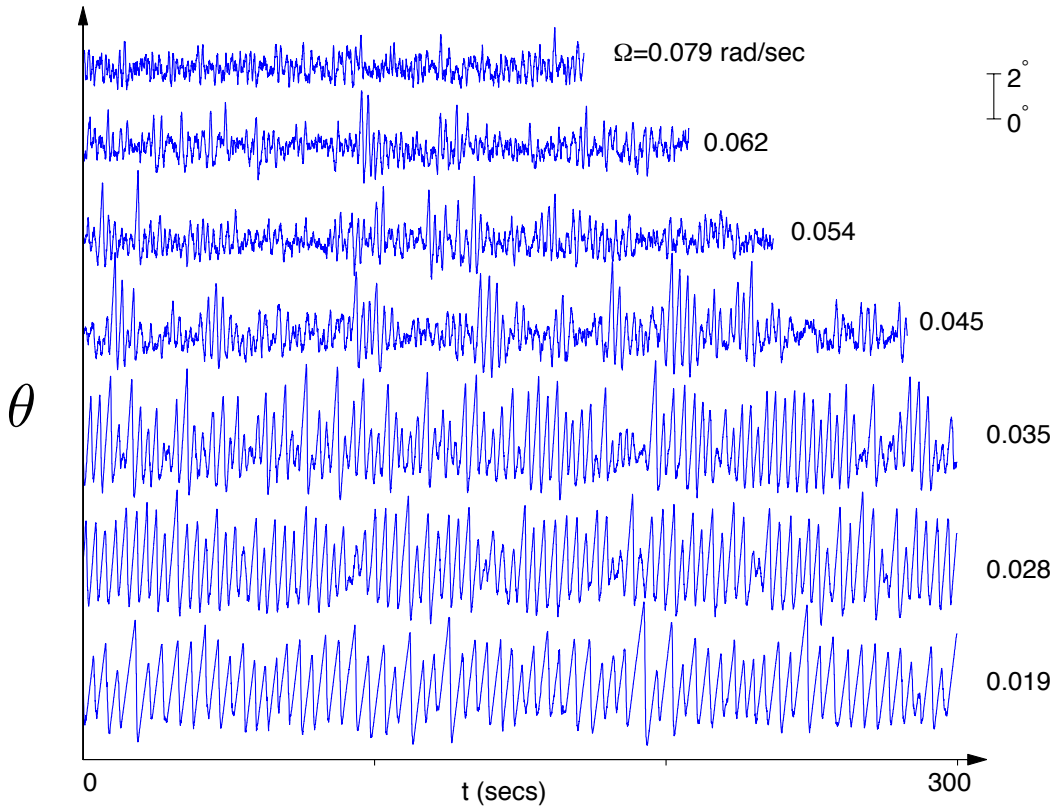

Figure 2: Representative time traces of θ at various rotation rates Ω measured in the Vancouver drum with 2 mm glass beads. At the lowest rotation rate ($\Omega = 0.019$ rad/sec) the system exhibits episodic avalanching. At the highest rotation rate ($\Omega = 0.079$ rad/sec) the system exhibits continuous flow. At intermediate flow rates the system exhibits both regimes in varying proportion.

time traces we extract the local maxima and local minima, and from these we calculate the average local maximum $\theta_{\max}$ and average local minimum $\theta_{\min}$. We also calculate the total time average θ which we denote $\langle\theta\rangle$.

The data shows the signature of the two regimes of granular flow. At the lowest rotation rate ($\Omega = 0.019$ rad/sec) the system exhibits pure avalanching with no regions of continuous flow. At the highest rotation rate ($\Omega = 0.079$ rad/sec) the system exhibits pure continuous flow with no avalanching. And at all intermediate rotation rates shown in Figure 2, the system intermittently transitions between avalanching and continuous flow.

In the episodic avalanching regime the mass of beads rotates as a solid body with the

drum until the pile reaches a critical angle θ_{start}, at which an avalanching layer of beads starts to flow. The avalanche stops when the angle of the pile reaches a second, lower critical angle θ_{stop}. These critical angles are reflected in the distinct and well-defined maximum and minimum pile angles θ_{max} and θ_{min}. We observe that θ_{max} and θ_{min} are independent of flow rate far from the transition to continuous flow for both the sand and the 3 mm glass beads.

In the continuous flow regime there is a continuously flowing layer of beads on the surface of the bead pile supported by the static, solidly rotating bulk. Far from the transition between episodic avalanching and continuous flow, the angle of the surface of the flowing layer remains relatively constant and stable in time, and the average angle of the pile increases as the flow rate increases. At low rotation rates which are just above the transition between episodic avalanching regime, the shape of the surface is almost linear. As the rotation rate increases, however, the surface begins to take on an "$\mathcal{S}$" shape. This effect is pronounced for thinner drums and there is good reason to believe it is due to the friction exerted on the flowing layer by the walls [15].

3.2 The transition between regimes: hysteresis and intermittency

Figure 3 shows plots of θ_{min}, $\langle\theta\rangle$, and θ_{max} against the flow rate $Q = \frac{1}{2}\Omega R^2$ for (A) 3 mm glass beads and (B) decorative aquarium sand. When the flow rate is very small or very

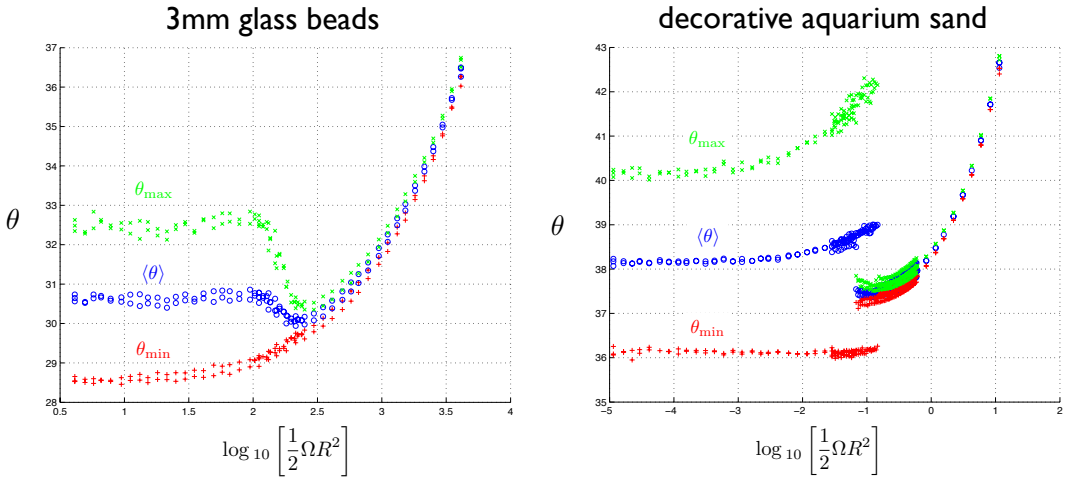

Figure 3: θ_{max}, $\langle\theta\rangle$, and θ_{min} for 3mm glass beads (left) and decorative aquarium sand (right) in the Vancouver drum for $W = 17\,\text{mm}$. Both materials exhibit episodic avalanching at low flow rates and continuous flow at high flow rates. (Left) the 3mm beads exhibit intermittent transition between avalanching and continuous flow for intermediate flow rates. (Right) the decorative aquarium sand exhibits hysteresis near the transition between avalanching and continuous flow, and no intermittency. The hysteric region was characterized thoroughly which is why there are more data points near transition.

large, the two materials exhibit qualitatively similar behavior. Overall, the sand has a significantly larger pile angle, which reflects its greater effective internal friction coefficients

and may be due to both to the irregular shape of the sand particles and greater interparticle friction forces. Both the glass beads and the sand exhibit two distinct regimes of granular flow: episodic avalanching at low flow rates, and continuous flow at high flow rates. When the pile angle θ is plotted against the flow rate Q, the signature of the avalanching regime is the widely disparate $\theta_{\min}$, $\langle\theta\rangle$, and $\theta_{\max}$. Far from the transition between avalanching and continuous flow these are independent of flow rate.

Close to the transition between episodic avalanching and continuous flow, however, the two materials exhibit qualitatively *different* behavior. For sand, there appears to be a sharp transition in θ between the continuous flow and avalanching regime. Furthermore, there is a range of flow rates for which both episodic avalanching and continuous flow is observed. In this regime we observe hysteresis; when the flow rate is increased from the avalanching regime, the system will remain in the avalanching regime until some critical maximum flow rate, and conversely for decreasing flow rate while in the continuous flow regime. Also, near the transition between the two regimes, the maximum θ for sand increases. This is because at high rotation speeds the pile angle continues to increase past θ_{start} even after the avalanche has been initiated. The same phenomenon is observed in $\theta_{\min}$.

For glass beads the transition between regimes exhibits smooth trends in $\theta_{\min}$, $\langle\theta\rangle$, and $\theta_{\max}$. This is consequence of the existence of intermittent transitions between episodic avalanching and continuous flow in this regime. These intermittent transitions are visible in the time traces plotted in Figure 2 for all but the largest and smallest rotation rates shown. The persistence time of either state before transition is dependent on the flow rate: when the flow rate is increased, the fraction of time that the system occupies the continuous flow state increases until the avalanching regime disappears altogether. Thus a smooth transition in pile angle is observed [4].

3.3 The importance of width

The pile angle is sensitive to the width of the drum when the width of the drum is smaller than the radius ($W/R \ll 1$). We observe a width dependence in the average pile angle for both the continuously flowing regime and avalanching regimes, as well as in critical angles θ_{start} and θ_{stop} for the avalanching regime. Figure 4 plots the average pile angle in the Vancouver drum for five different widths and compares the results. In the Vancouver drum we see that when $W \geq 110\,\text{mm}$ the width is no longer important.

3.4 Comparison of Woods Hole and Vancouver

Figure 5 compares the results from the Woods Hole and Vancouver drums with 3 mm glass spheres for various widths. We see that when the results for $\langle\theta\rangle$ collapse for the Woods Hole and Vancouver drums for three widths when plotted against the flow rate $Q = \frac{1}{2}\Omega R^2$. It appears therefore that even to $W/R \approx 1$ the inclination of the surface is controlled by the drum width. We note that the narrowest width in the Woods Hole drum was measured closer to 18 mm, but despite this slight difference between Woods Hole and Vancouver the data collapses impressively.

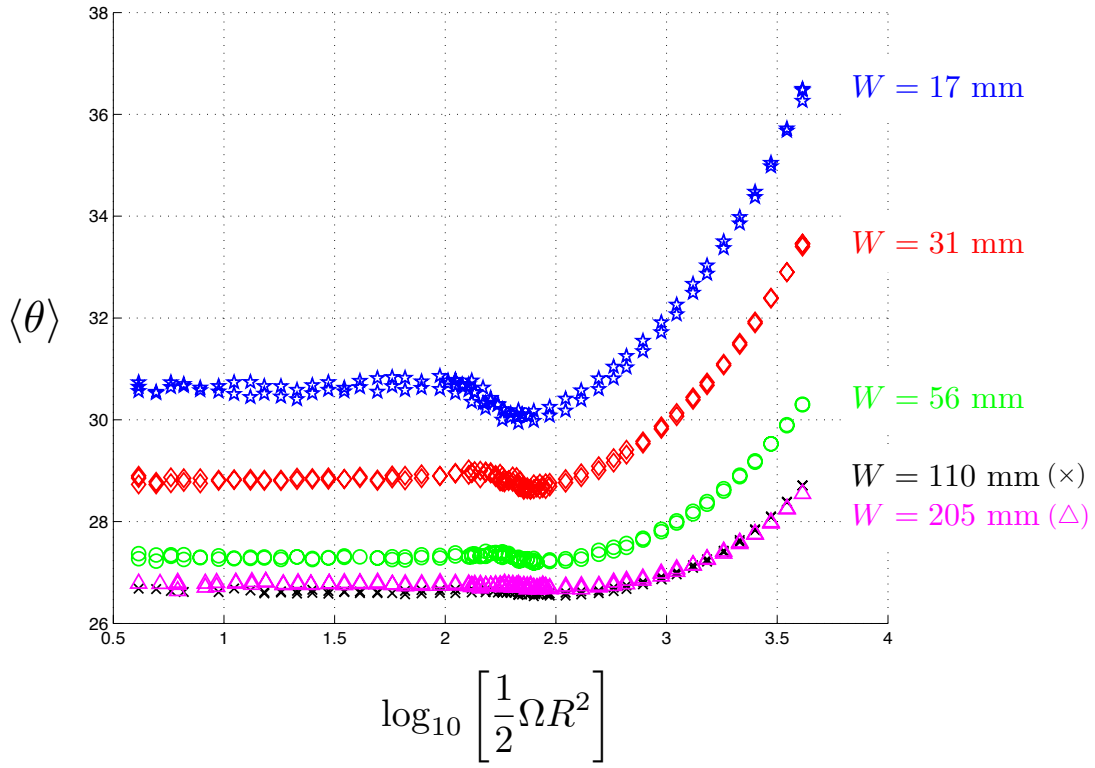

Figure 4: Average pile angle for five different widths in the Vancouver drum ($R = 144\,\text{mm}$). ($\star$, blue) $W = 17\,\text{mm}$, ($\diamond$, red) $W = 31\,\text{mm}$, ($\bigcirc$, green), $W = 56\,\text{mm}$, ($\times$, black) $W = 110\,\text{mm}$, ($\triangle$, magenta) $W = 205\,\text{mm}$. The pile angle decreases as the width increases for small W/R. When W is comparable to R the pile angle appears to saturate and the width is no longer important.

4 Theory

We now attempt to develop a theoretical explanation for the observed behavior of the system. Our ultimate hope is to develop an explanation for the transition between episodic avalanching and continuous flow. We start by developing a model for the continuously flowing layer in narrow drums which relies on the fact that the width of the drum is the controlling parameter. The basis of our description is the continuum assumption and the conservation of mass and momentum for an incompressible granular fluid,

$$\nabla \cdot \mathbf{u} = 0, \tag{1}$$

$$\rho \frac{D\mathbf{u}}{Dt} = -\nabla p + \nabla \cdot \boldsymbol{\tau} + \rho \mathbf{g}, \tag{2}$$

where $\mathbf{u} = \{u, v, w\}$ is the velocity of the granular material, ρ is the bulk density, p is an isotropic pressure, $\boldsymbol{\tau}$ (τ_{ij} in indicial notation) is the deviatoric stress tensor, and $\mathbf{g}$ is gravitational acceleration. To relate the state of the system to the internal deviatoric stress τ_{ij} we employ the empirical "$\mu(I)$" law, where $\mu(I)$ is an effective friction coefficient of

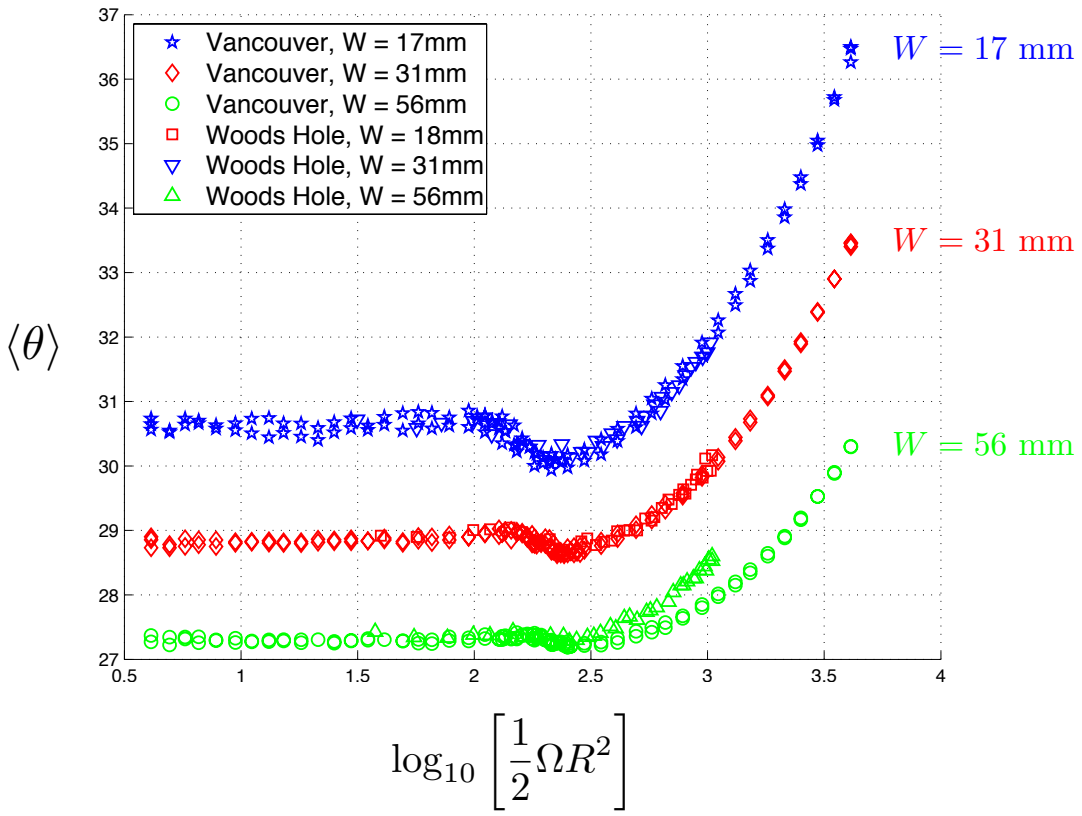

Figure 5: Comparison of the average pile angle for Woods Hole ($R = 69\,\text{mm}$) and Vancouver ($R = 144\,\text{mm}$) drums for three widths W. ($\star$, blue) Vancouver with $W = 17\,\text{mm}$, ($\triangledown$, blue) Woods Hole with $W = 18\,\text{mm}$, ($\diamond$, red) Vancouver with $W = 31\,\text{mm}$, ($\square$, red) Woods Hole with $W = 31\,\text{mm}$. ($\bigcirc$, green) Vancouver with $W = 56\,\text{mm}$, ($\triangle$, green) Woods Hole with $W = 56\,\text{mm}$. We see the observed pile angles appear to be controlled by the width of the drum even to when $W/R \approx 1$ (for the Woods Hole drum with $W = 56\,\text{mm}$): the pile angles collapse for Woods Hole and Vancouver when plotted against flow rate $Q = \frac{1}{2}\Omega R^2$.

proportionality between the deviatoric stress and the pressure, or normal force such that [9],

$$\tau_{ij} = \mu(I) p \frac{\dot{\gamma}_{ij}}{|\dot{\gamma}|}, \tag{3}$$

where $\dot{\gamma}_{ij}$ is the rate of strain tensor and I is the "inertia number". The inertia number is defined

$$I = \frac{|\dot{\gamma}| d}{\sqrt{p/\rho}}, \tag{4}$$

where $|\dot{\gamma}| = \sqrt{\frac{1}{2}\dot{\gamma}_{ij}\dot{\gamma}_{ij}}$ is the second invariant of $\dot{\gamma}_{ij}$ and d is particle diameter. The inertia number can be interpreted as the ratio of two characteristic timescales in the relative motion of two grain layers: kinematic T_{kin} and mechanical T_{mech} [10]. The kinematic timescale is a

characteristic timescale for the relative motion of the grain layers,

$$T_{\text{kin}} = \frac{d}{V_{\text{kin}}} = \frac{d}{d|\dot{\gamma}|} = \frac{1}{|\dot{\gamma}|}, \tag{5}$$

where V_{kin} is the relative velocity of the grain layers. The mechanical timescale is a characteristic timescale for the acceleration of the layers a_{mech} due to mechanical forces exerted on the layer,

$$T_{\text{mech}} = \sqrt{\frac{d}{a_{\text{mech}}}} = \sqrt{\frac{d}{F/m}} = \sqrt{d\,\frac{\rho dA}{pA}} = d\sqrt{\frac{\rho}{p}}, \tag{6}$$

where A is the area of the layer, $F = pdL$ is the normal force exerted on the layer due to the pressure p, and $m = \rho d^2 L$ is the mass of the layer. The ratio of these timescales is the inertia number,

$$I = \frac{T_{\text{mech}}}{T_{\text{kin}}} = \frac{|\dot{\gamma}|d}{\sqrt{p/\rho}}. \tag{7}$$

When the inertia number is large, the rate of deformation of the granular medium is fast relative to the rate of displacement of the medium due to mechanical forces. Experiments in shear cells and on inclined planes show that the effective friction coefficient μ collapses to a single curve when plotted against I [5]. We see that the effective coefficient has some finite value μ_1 at $I = 0$ and asymptotes to a second limiting value μ_2 as $I \to \infty$. To capture this dependence we use the formula [9]

$$\mu(I) = \mu_1 + (\mu_2 - \mu_1)\,\frac{I}{I + I_0}, \tag{8}$$

where I_0 is a material parameter which characterizes how quickly $\mu(I)$ transitions between its lower and upper values with increasing I. These equations serve as a starting point for the derivation of approximate models for granular flow in the rotating drum.

4.1 Thin, Shallow, Slippy

For our first attempt to model the flowing layer we reduce the full conservation equations greatly through a series of approximations and assumptions. We assume that the width and depth of the flow are much smaller than it's length, that we can neglect inertia, and that the internal friction coefficient $\mu(I)$ and the friction coefficient between the flowing beads and the wall are small. With these assumptions we are able to derive a single partial differential equation for the height profile of the flowing layer which is easily solved numerically. The derived model, which we call the "thin, shallow, slippy' model, or "TSS" then represents the leading order system of equations in a formal asymptotic expansion. The derivation of the model from the full detailed conservation laws illustrates clearly its approximations and limitations.

4.1.1 The momentum equation

We start by defining the characteristic dimensions for the flow: length R, depth H, and width W. A schematic of the drum, the flowing layer, and coordinate system is shown

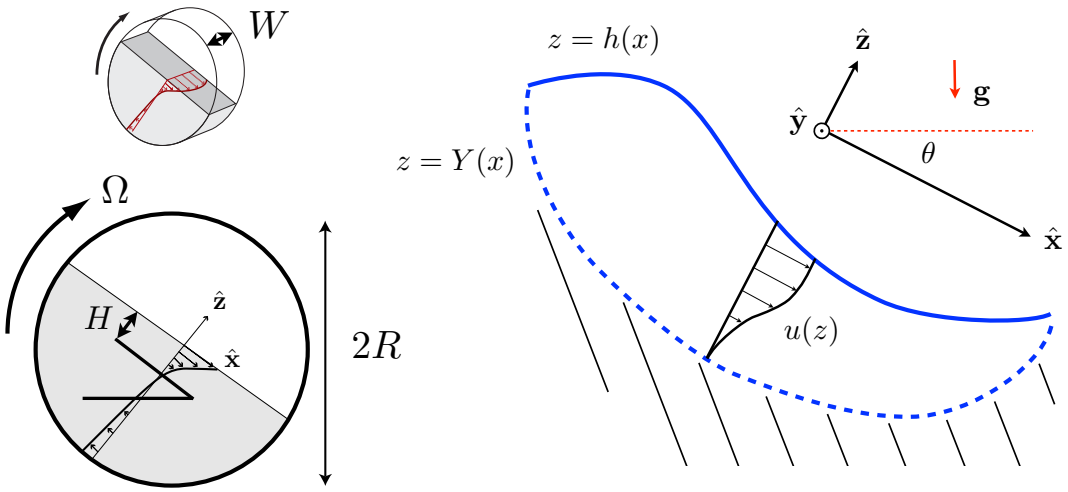

Figure 6: A schematic of the drum illustrating the characteristic dimensions and showing the coordinate system. The radius of the drum is R, the (average or characteristic) depth of the flowing layer is H, and the width of the drum is W. The surface of the flowing layer is defined at $z = h(x)$ and the yield surface dividing the flowing layer and the static bed of grains beneath is defined at $z = Y(x)$. The coordinate system is tilted at an angle θ with respect to the vertical as defined by the direction of gravity.

in Figure 6. We assume that the flow is thin and shallow such that $\epsilon = H/R \ll 1$ and $\Delta = W/H \ll 1$. These yield scalings for u, v, and w through the mass conservation equation, and from these we find scalings for $\dot{\gamma}_{ij}$ and τ_{ij}. If we substitute

$$x = Rx', \qquad y = Wy', \qquad z = Hz', \qquad u = Uu', \qquad v = Vv', \qquad w = \mathbb{W}w', \tag{9}$$

where U, V, and $\mathbb{W}$ are characteristic velocities and the primes denote a non-dimensional quantity. The mass conservation equation (1) then becomes

$$\left(\frac{U}{R}\right)\frac{\partial u'}{\partial x'} + \left(\frac{V}{W}\right)\frac{\partial v'}{\partial y'} + \left(\frac{\mathbb{W}}{H}\right)\frac{\partial w'}{\partial z'} = 0. \tag{10}$$

For each term to be of comparable magnitude, we must have that $V \sim \epsilon\Delta U$ and $\mathbb{W} \sim \epsilon U$. Next we need to non-dimensionalize the pressure and deviatoric stress tensor. We assume that the pressure is hydrostatic, which implies that

$$p = \rho g H p'. \tag{11}$$

The deviatoric stress tensor is defined as $\tau_{ij} = \mu(I)p\dot{\gamma}_{ij}/|\dot{\gamma}|$, so we need to analyze the rate of strain tensor $\dot{\gamma}_{ij}$ in order to non-dimensionalize it properly. The rate of strain tensor is defined as

$$\dot{\gamma}_{ij} = \begin{pmatrix} 2u_x & u_y + v_x & u_z + w_z \\ u_y + v_x & 2v_y & v_z + w_y \\ u_z + w_z & v_z + w_y & 2w_z \end{pmatrix}, \tag{12}$$

where we are using the shorthand $u_x = \partial u/\partial x$ here for compactness. Introducing our scalings we find

$$\dot{\gamma}_{ij} = \frac{U}{H}\begin{pmatrix} 2\epsilon u_x & \frac{1}{\Delta}u_y + \epsilon^2\Delta v_x & u_z + \epsilon^2 w_z \\ \frac{1}{\Delta}u_y + \epsilon^2\Delta v_x & 2\epsilon v_y & \epsilon\Delta v_z + \frac{\epsilon}{\Delta}w_y \\ u_z + \epsilon^2 w_z & \epsilon\Delta v_z + \frac{\epsilon}{\Delta}w_y & 2\epsilon w_z \end{pmatrix}. \tag{13}$$

We see therefore that in order for the flow to be two-dimensional at leading order, we need to assume that the y-dependence in the velocity is at most a correction at order Δ^2, or that

$$\mathbf{u}(x,y,z,t) = \mathbf{u}^{(0)}(x,z,t) + \Delta^2\mathbf{u}^{(2)}(x,y,z,t). \tag{14}$$

If we assume this then we find for $\dot{\gamma}_{ij}$,

$$\dot{\gamma}_{ij} = \frac{U}{H}\begin{pmatrix} 2\epsilon u_x & \Delta u_y + \epsilon^2\Delta v_x & u_z + \epsilon^2 w_z \\ \Delta u_y + \epsilon^2\Delta v_x & 2\epsilon\Delta^2 v_y & \epsilon\Delta v_z + \epsilon\Delta w_y \\ u_z + \epsilon^2 w_z & \epsilon\Delta v_z + \epsilon\Delta w_y & 2\epsilon w_z \end{pmatrix}. \tag{15}$$

Keeping in mind that the second invariant is $|\dot{\gamma}| = \sqrt{\frac{1}{2}\dot{\gamma}_{ij}\dot{\gamma}_{ij}}$ we then non-dimensionalize each component of τ_{ij},

$$(\tau_{xx}, \tau_{zz}) = \widehat{\mu}\rho g H\epsilon\left(\tau'_{xx}, \tau'_{zz}\right), \qquad \tau_{yy} = \widehat{\mu}\rho g H\epsilon\Delta^2\tau'_{yy}, \tag{16}$$

$$\tau_{xy} = \widehat{\mu}\rho g H\Delta\tau'_{xy} \qquad \tau_{yz}, = \widehat{\mu}\rho g\epsilon\Delta\tau'_{yz}, \qquad \tau_{xz} = \widehat{\mu}\rho g H\tau'_{xz}, \tag{17}$$

where we have substituted $\mu(I) = \widehat{\mu}\mu'$ so that $\widehat{\mu}$ represented the magnitude of $\mu(I)$. Inserting these scalings into the momentum conservation equations yields

$$\mathrm{Fr}\frac{Du}{Dt} = -\epsilon\frac{\partial p}{\partial x} + \sin\theta + \widehat{\mu}\left(\epsilon^2\frac{\partial \tau_{xx}}{\partial x} + \frac{\partial \tau_{xy}}{\partial y} + \frac{\partial \tau_{xz}}{\partial z}\right), \tag{18}$$

$$\epsilon\Delta\mathrm{Fr}\frac{Dv}{Dt} = -\frac{\partial p}{\partial y} + \widehat{\mu}\left(\epsilon\frac{\partial \tau_{xy}}{\partial x} + \epsilon\Delta\frac{\partial \tau_{yy}}{\partial y} + \epsilon\frac{\partial \tau_{yz}}{\partial z}\right), \tag{19}$$

$$\epsilon\mathrm{Fr}\frac{Dw}{Dt} = -\frac{\partial p}{\partial z} - \cos\theta + \widehat{\mu}\left(\epsilon\frac{\partial \tau_{xz}}{\partial x} + \epsilon\frac{\partial \tau_{yz}}{\partial y} + \epsilon\frac{\partial \tau_{zz}}{\partial z}\right), \tag{20}$$

where we have defined the Froude number $\mathrm{Fr} = U^2/gH$. If we assume that inertia is negligible such that $\mathrm{Fr} \ll 1$ and $\{\widehat{\mu}, \theta\} = O(\epsilon)$ (a fair assumption for many materials for which $\mu(I) \approx 0.2$–0.4), the leading order equations with dimensionality restored are

$$0 = -\frac{\partial p}{\partial x} + \rho g\sin\theta + \frac{\partial \tau_{xy}}{\partial y} + \frac{\partial \tau_{xz}}{\partial z}, \tag{21}$$

$$0 = -\frac{\partial p}{\partial y}, \tag{22}$$

$$0 = -\frac{\partial p}{\partial z} - \rho g\cos\theta. \tag{23}$$

In other words, we have that the pressure is hydrostatic, and that the x–momentum is a balance between lateral and vertical shear-induced friction, gravity, and the pressure which will come in to the equations as a shallow-water-like term dependent on the height of the flowing layer.

4.1.2 Boundary conditions

To proceed with the model we need boundary conditions at the sidewalls, at the material free surface forming the upper boundary of the flowing layer, and at the yield surface forming the lower boundary. The stress at the sidewalls is modeled as an effective friction force which opposites the velocity of the flowing layer there,

$$\boldsymbol{\tau} \cdot \mathbf{n} = \mu_{\mathrm{w}} p \frac{u\widehat{\mathbf{e}}_x + w\widehat{\mathbf{e}}_z}{\sqrt{u^2+w^2}} \left(\mathbf{n} \cdot \widehat{\mathbf{e}}_y\right), \tag{24}$$

where μ_{w} is the effective friction coefficient between the flowing beads and the wall and $\mathbf{n}$ is the surface normal which points into the flowing layer. At the confining sidewalls at $y = 0$ and $y = W$ we therefore have that

$$\tau_{xy}\big|_{y=0} = \mu_{\mathrm{w}} p \,\mathrm{sgn}(u) \qquad \text{and} \qquad \tau_{xy}\big|_{y=W} = -\mu_{\mathrm{w}} p \,\mathrm{sgn}(u). \tag{25}$$

It was observed by de Ryck and Louisnard [2] that in the case of very rough walls with a large friction coefficient we would expect to find a stationary monolayer of beads adjacent to the wall such that the effective friction coefficient between the flowing layer and the wall would simply be μ_1. This implies that μ_{w} has the constraint $\mu_{\mathrm{w}} \leq \mu_1$.

At the top of the flowing layer we define the material free surface as $z = h(x)$. Here we assume that the same free surface boundary conditions used for common fluids like water are applicable, or that,

$$p\big|_{z=h} = 0 \qquad \text{and} \qquad \tau_{xz}\big|_{z=h} = 0. \tag{26}$$

The base of the layer is a yield surface which we define as $z = Y(x)$. At this boundary the velocity of the beads equals the velocity of the beads in the static layer which rotate with the drum, or that

$$\mathbf{u}\big|_{z=Y} = u_{\widetilde{\theta}} \widehat{\mathbf{e}}_{\widetilde{\theta}}, \tag{27}$$

where $\widetilde{\theta}$ is the angle associated with the coordinate (x, Y) in the rotated coordinate frame. The tangential velocity $u_{\widetilde{\theta}}$ is simply Ωr, where Ω is the rotation rate of the drum and r is the radial position. We therefore have

$$u\big|_{z=Y} = u_{\widetilde{\theta}} \sin\widetilde{\theta} = \Omega Y, \tag{28}$$

$$w\big|_{z=Y} = u_{\widetilde{\theta}} \cos\widetilde{\theta} = -\Omega x. \tag{29}$$

If we non-dimensionalize each velocity at the boundary with ΩR such that $u = \Omega R u'$ and $Y = HY'$ we find

$$u'\big|_{z=Y} = \epsilon Y', \tag{30}$$

and so in our leading order approximation the boundary conditions at the yield surface $z = Y(x)$ are

$$u\big|_{z=Y} = 0 \qquad \text{and} \qquad w\big|_{z=Y} = -\Omega x. \tag{31}$$

4.1.3 Depth-averaged mass conservation equation

We can simplify our system of equations further by using the depth-averaged mass conservation equation commonly used for thin layers. To find this equation we first average the continuity equation across the width of the drum. Using our assumption that the flow is two-dimensional to leading order in Δ (14) and impermeability at the drum walls, we find

$$\begin{aligned} 0 &= \frac{1}{W}\int_0^W \left[\frac{\partial u}{\partial x} + \frac{\partial v}{\partial y} + \frac{\partial w}{\partial z}\right] \mathrm{d}y, \\ &= \frac{\partial u}{\partial x} + \frac{\partial w}{\partial z} + \frac{1}{W}\left(v\,\big|_{y=W} - v\,\big|_{y=0}\right), \\ &= \frac{\partial u}{\partial x} + \frac{\partial w}{\partial z}. \end{aligned} \tag{32}$$

We then integrate in z from the yield surface at $z = Y(x)$ to the upper material free surface at $z = h(x)$,

$$\int_Y^h \left[\frac{\partial u}{\partial x} + \frac{\partial w}{\partial z}\right] \mathrm{d}z = 0. \tag{33}$$

At $z = Y$ we have that $u = 0$ and $w = -\Omega x$. At $z = h$, which is a material surface, we have the kinematic condition which requires

$$w\,\big|_{z=h} = \frac{\partial h}{\partial t} + u\,\big|_{z=h}\frac{\partial h}{\partial x}. \tag{34}$$

We use Leibnitz's rule and the boundary condition at $z = Y$ to identify

$$\int_Y^h \frac{\partial u}{\partial x}\,\mathrm{d}z = \frac{\partial}{\partial x}\int_Y^h u\,\mathrm{d}z - \frac{\partial h}{\partial x}u\,\big|_{z=h} + \frac{\partial Y}{\partial x}u\,\big|_{z=Y} = \frac{\partial}{\partial x}\int_Y^h u\,\mathrm{d}z - \frac{\partial h}{\partial x}u\,\big|_{z=h}. \tag{35}$$

Noting that $\int_Y^h u\,\mathrm{d}z = Q(x)$ is the width-specific flux, we find

$$\begin{aligned} 0 &= \frac{\partial}{\partial x}\int_Y^h u\,\mathrm{d}z - \frac{\partial h}{\partial x}u(z=h) + \frac{\partial Y}{\partial x}u(z=Y) + w(z=h) - w(z=Y), \\ &= \frac{\partial h}{\partial t} + \frac{\partial Q}{\partial x} + \Omega x, \end{aligned} \tag{36}$$

which we write

$$\frac{\partial h}{\partial t} + \frac{\partial Q}{\partial x} = -\Omega x. \tag{37}$$

Furthermore, we place the origin of the coordinate system at the center of the drum. When the drum is half-filled and we neglect any changes in volume fraction of the flowing grains, the total conservation of granular material along with our choice of origin implies that

$$\int_{-R}^{R} h(x)\,\mathrm{d}x = 0. \tag{38}$$

Another way to state this condition is that the addition of material in one part of the drum requires a subtraction of material elsewhere.

4.1.4 Width-averaged momentum equation

To simplify the x–momentum equation further we observe that our "2D" assumption that the $y-$dependence of u is at most a correction of $O(\Delta^2)$ permits us to average the x–momentum equation in y. This leaves all terms unchanged except for $\partial\tau_{xy}/\partial y$, which is replaced by the boundary conditions at either bounding wall. Because the velocity is unidirectional we find

$$\frac{1}{W} = \int_0^W \frac{\partial \tau_{xy}}{\partial y}\,\mathrm{d}y = \frac{1}{W}\left(\tau_{xy}\,\big|_{y=W} - \tau_{xy}\,\big|_{y=0}\right) = -2\delta p, \tag{39}$$

where we have defined the wall friction parameter $\delta = \mu_\mathrm{w}/W$ is the friction coefficient between the flowing bead layer and the sidewall. The other terms in the x-momentum equation are unchanged and so it becomes

$$0 = -\frac{\partial p}{\partial x} + \rho g \sin\theta - 2\delta p + \frac{\partial \tau_{xz}}{\partial z}. \tag{40}$$

4.1.5 A note on θ

In the theory, we have defined θ as the inclination of our coordinate system, while in the experiments θ is defined by a linear fit to its surface in the cropped region of the image in Figure 1(D). In the solution of the model, we found that is was slightly more convenient to define the inclination of the coordinate system as the *average* inclination of the slope, rather than the inclination of the slope over some region of the surface in the center of the drum. Despite the confusion caused by the different definitions, it seems that these θ are nevertheless approximately the same. The definition that θ in the model is the average slope of the surface implies that $h(x)$ must satisfy

$$\frac{1}{2R}\int_{-R}^{R} \frac{\partial h}{\partial x}\,\mathrm{d}x = \frac{1}{2R}\left(h(R) - h(-R)\right) = 0. \tag{41}$$

4.2 Solution of TSS

To solve the TSS model we first observe that Equation (23) implies that pressure is hydrostatic, or

$$p = \rho g \cos\theta (h - z), \tag{42}$$

where we have applied the boundary condition $p\,|_{z=h} = 0$. Inserting this into the width-averaged x–momentum equation (40) yields

$$0 = -\rho g \cos\theta \frac{\partial h}{\partial x} + \rho g \sin\theta - 2\delta\rho g \cos\theta (h - z) + \frac{\partial \tau_{xz}}{\partial z}. \tag{43}$$

Rearranging and integrating from z to h yields

$$\tau_{xz} = -\rho g \cos\theta (h - z)\left[h_x - \tan\theta + \delta(h - z)\right]. \tag{44}$$

We note that to leading order $\tau_{xz} = \mu(I)p = \mu(I)\rho g\cos\theta(h-z)$, which implies

$$\mu(I) = -h_x + \tan\theta - \delta(h - z). \tag{45}$$

The definition of $\mu(I)$ is

$$\mu(I) = \mu_1 + (\mu_2 + \mu_1)\,\frac{I}{I + I_0}, \tag{46}$$

and substitution this into Equation (45) and solving for I yields

$$I = I_0 \left[\frac{\tan\theta - \mu_1 - h_x - \delta(h - z)}{\mu_2 - \tan\theta + h_x + \delta(h - z)}\right]. \tag{47}$$

We can write this in a simpler way in terms of the yield surface $z = Y$. In order for the granular material to flow we must have that the shear stress exceeds $\mu_1 p$, or that

$$\tau_{xz} > \mu_1 p. \tag{48}$$

This implies that in the flowing layer we have

$$-h_x + \tan\theta - \delta(h - z) > \mu_1, \tag{49}$$

and that the yield surface $z = Y$ is defined by

$$Y = h - \frac{\tan\theta - \mu_1 - h_x}{\delta}. \tag{50}$$

We can therefore rewrite the relation for I as

$$I = I_0 \left[\frac{\delta(z - Y)}{\Delta\mu - \delta(z - Y)}\right], \tag{51}$$

where we have defined $\Delta\mu = \mu_2 - \mu_1$. To leading order we have

$$I = \frac{|\dot{\gamma}|d}{\sqrt{p/\rho}} = \frac{u_z d}{\sqrt{g\cos\theta(h - z)}}, \tag{52}$$

and combining this with (51) and rearranging provides an equation for $\partial u/\partial z$,

$$\frac{\partial u}{\partial z} = \frac{\delta I_0\sqrt{g\cos\theta}}{d\Delta\mu}\left[\frac{\sqrt{h - z}(z - Y)}{1 - \frac{\delta}{\Delta\mu}(z - Y)}\right]. \tag{53}$$

With this equation we are then able to calculate the flow rate Q and are then in a position to solve the depth-averaged momentum equation. To calculate $Q = \int u\,\mathrm{d}z$, we first observe that through integration by parts,

$$\int_Y^h (h - z)\frac{\partial u}{\partial z}\,\mathrm{d}z = u(h - z)\Big|_Y^h + \int_Y^h u\,\mathrm{d}z = Q, \tag{54}$$

which means that we have to calculate only one integral for Q,

$$Q = \frac{\delta I_0\sqrt{g\cos\theta}}{d}\int_Y^h \frac{(h - z)^{3/2}\,(z - Y)}{\Delta\mu - \delta(z - Y)}\,\mathrm{d}z. \tag{55}$$

This integral can be calculated analytically. We find

$$Q = \frac{2I_0\sqrt{g\cos\theta}}{d}\left(\frac{\Delta\mu}{\delta}\right)^{5/2} q\left(\frac{\tan\theta - \mu_1 - h_x}{\Delta\mu}\right), \tag{56}$$

where

$$q(s) = (1-s)\left[\sqrt{1-s}\tan^{-1}\left(\sqrt{\frac{s}{1-s}}\right) - \sqrt{s} + \frac{1}{3}s^{3/2}\right] + \frac{2}{15}s^{5/2}. \tag{57}$$

Note that

$$q(s \to 0) \approx \frac{2}{35}s^{7/2} + O\left(s^{9/2}\right). \tag{58}$$

From the expression for $q(s)$ we see that s cannot be greater than 1, or that $\tan\theta - h_x$ cannot be greater than μ_2. This reflects our assumption that inertia is negligible and the flow is not accelerating. If $\tan\theta - h_x > \mu_2$, then the pile is too steep for friction forces to balance gravitational forces and the flow must accelerate. Further, we can easily calculate that $q(s=1) = 2/15$, which implies that

$$\frac{d\Omega R^2}{4I_0\sqrt{g\cos\theta}}\left(\frac{\delta}{\Delta\mu}\right)^{5/2} < \frac{2}{15}, \tag{59}$$

for the existence of a solution without taking into account inertial terms.

This expression for Q yields a partial differential equation for $h(x,t)$ when inserted into the depth-averaged mass conservation equation (37). The steady solution satisfies

$$\frac{\partial Q}{\partial x} = -\Omega x. \tag{60}$$

The impermeability boundary condition at the boundaries of the drum require that $u\,|_{x=\pm R} = 0$, which implies that

$$Q\,\big|_{x=\pm R} = 0. \tag{61}$$

Integrating Equation (60) from $x = -R$ to x yields

$$Q = \frac{1}{2}\Omega\left(R^2 - x^2\right) = \frac{\Omega R^2}{2}\left(1 - \left(\frac{x}{R}\right)^2\right). \tag{62}$$

The general steady problem is then to solve the nonlinear ordinary differential equation

$$q\left(\frac{\tan\theta - \mu_1 - h_x}{\Delta\mu}\right) = \frac{\Omega R^2 d}{4I_0\sqrt{g\cos\theta}}\left(\frac{\delta}{\Delta\mu}\right)^{5/2}\left(1 - \left(\frac{x}{R}\right)^2\right), \tag{63}$$

under the constraint that

$$\int_{-R}^{R} h(x)\,\mathrm{d}x = 0. \tag{64}$$

4.2.1 The "low-flux" limit

The problem is simplified in the limit when $s = \frac{1}{\Delta\mu}(\tan\theta - \mu_1 - h_x)$ in $q(s)$ is small. We have $q(s \to 0) = (2/35)s^{7/2} + O(s^{9/2})$, which means that

$$\frac{2}{35}\left(\frac{\tan\theta - \mu_1 - h_x}{\Delta\mu}\right)^{7/2} = \frac{\Omega R^2 d}{4I_0\sqrt{g\cos\theta}}\left(\frac{\delta}{\Delta\mu}\right)^{5/2}\left(1 - \left(\frac{x}{R}\right)^2\right). \tag{65}$$

Solving for h_x, we find,

$$\frac{\partial h}{\partial x} = \tan\theta - \mu_1 - \Delta\mu\left(\frac{35\Omega R^2 d}{8I_0\sqrt{g\cos\theta}}\right)^{2/7}\left(\frac{\delta}{\Delta\mu}\right)^{5/7}\left(1 - \left(\frac{x}{R}\right)^2\right)^{2/7}. \tag{66}$$

A single integration yields $h(x)$,

$$\begin{aligned} h(x) - h(-R) = {} & \tan\theta - \mu_1 (x + R) \\ & - \Delta\mu\left(\frac{35\Omega R^2 d}{8I_0\sqrt{g\cos\theta}}\right)^{2/7}\left(\frac{\delta}{\Delta\mu}\right)^{5/7}\int_{-R}^{x}\left(1 - \left(\frac{x'}{R}\right)^2\right)^{2/7}\,\mathrm{d}x', \end{aligned} \tag{67}$$

where $h(-R)$ is determined by the total conservation of mass expressed by Equation (64).

4.2.2 General solution

The function $q(s)$ cannot be inverted analytically, which means that without approximation we cannot find a closed-form expression for $\partial h/\partial x$. Thus we must turn to numerics. We can express the general problem given by Equation (63) by writing

$$q(s) = C\left(1 - \left(\frac{x}{R}\right)^2\right). \tag{68}$$

Our strategy is to map $q(s)$ as a function of s, invert the mapping, and then integrate the inverted mapping to find $h(x)$. If we substitute a function $x^*(s)$ for x in (68), we can write

$$x = \pm R\sqrt{1 - \frac{1}{C}q(s)}. \tag{69}$$

We then find numerically the x which correspond to all valid s, and therefore also $s(x)$ as a function of x. Formally then,

$$q^{-1}\left(C\left[1 - \left(\frac{x}{R}\right)^2\right]\right) = s(x) = \frac{1}{\Delta\mu}\left(\tan\theta - \mu_1 - \frac{\partial h}{\partial x}\right), \tag{70}$$

so

$$h(x) - h(-R) = (\tan\theta - \mu_1)(x + R) - \Delta\mu\int_{-R}^{x} s(x)\,\mathrm{d}x', \tag{71}$$

where condition (64) then yields $h(-R)$. In practice, we use MATLAB's `cumtrapz` to calculate the integral in (71) using the mapping between s and x and find the difference $h(x) - h(-R)$. Integrating this difference yields $h(-R)$, since (64) implies

$$h(-R) = -\frac{1}{2R}\int_{-R}^{R} h(x) - h(-R)\,\mathrm{d}x. \tag{72}$$

Finally, after finding $h(x)$ for this initial choice of θ, we must iterate until the condition (41) is met. An example of $h(x)$ is shown in Figure 7 in the rotated frame (A) and lab frame (B).

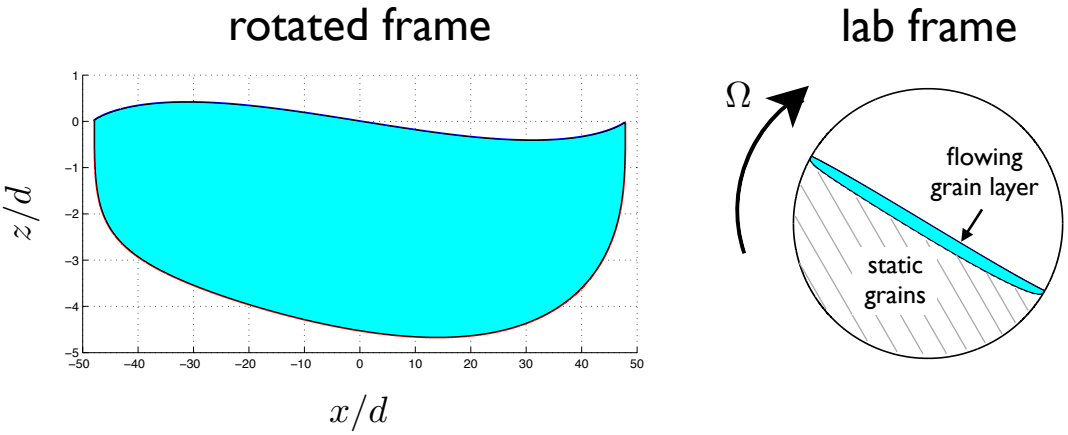

Figure 7: An example of the geometry of a predicted grain layer as defined by the upper free surface $h(x)$ and the lower yield surface $Y(x)$. (Left) the calculated geometry of the grain layer, shaded in blue, in the rotated frame with an exaggerated vertical dimension. (Right) the calculated geometry of the grain layer, shaded in blue, as it looks in the lab frame inserted into the drum.

4.3 Crude inertial model for avalanches

By neglecting inertial terms in the momentum equation, we preclude the possibility for avalanches, despite the fact that we might still consider time-dependent behavior by retaining the time-derivative in the depth-averaged continuity equation (37). More on why...

To consider inertia, we could solve the full equations, but this would involve significant computational effort. Instead we develop a crude "depth-averaged model" which, upon assuming a functional form for the velocity profile $u(z)$ that does not change in time or along the layer, yields a partial differential equation for the average velocity $U(x,t) = \frac{1}{h-Y}\int_Y^h u\,\mathrm{d}z$, and the height of the layer $h(x,t)$. If we use the same scaling as for the "thin, shallow, slippy" model, we still find from the z-momentum equation that pressure is hydrostatic,

$$p = \rho g \cos\theta (h - z). \tag{73}$$

However this time we retain all terms in the (y-averaged) x-momentum equation. Using the continuity equation we have the identity

$$\frac{\partial}{\partial x}\left(u^2\right) + \frac{\partial}{\partial z}(uw) = u\frac{\partial u}{\partial x} + u\frac{\partial w}{\partial z} + u\left(\frac{\partial u}{\partial x} + \frac{\partial w}{\partial z}\right) = u\frac{\partial u}{\partial x} + u\frac{\partial w}{\partial z}, \tag{74}$$

which means that the y-averaged x-momentum equation can be written

$$\rho\left(\frac{\partial u}{\partial t} + \frac{\partial}{\partial x}\left(u^2\right) + \frac{\partial}{\partial z}(uw)\right) = -p_x + \rho g \sin\theta - 2\delta p + \frac{\partial \tau_{xz}}{\partial z}. \tag{75}$$

Inserting hydrostatic pressure yields

$$\rho\left(\frac{\partial u}{\partial t}+\frac{\partial}{\partial x}\left(u^2\right)+\frac{\partial}{\partial z}\left(uw\right)\right)=\rho g\cos\theta\left(\tan\theta-h_x-2\delta(h-z)\right)+\frac{\partial\tau_{xz}}{\partial z}. \tag{76}$$

Integrating in z from $z=Y$ to $z=h$ and applying Leibniz's rule to remove derivatives from integrals yields

$$\rho\left[\frac{\partial}{\partial t}\int_b^h u\,\mathrm{d}z-\frac{\partial h}{\partial t}u(z=h)+\frac{\partial Y}{\partial t}u(z=b)\right]+\rho\left[\frac{\partial}{\partial x}\int_Y^h u^2\,\mathrm{d}z-\frac{\partial h}{\partial x}u^2(z=h)+\frac{\partial Y}{\partial x}u^2(z=Y)\right]\cdots$$
$$+\rho uw\Big|_{z=h}-\rho uw\Big|_{z=Y}=\rho g(h-Y)\cos\theta\left[\tan\theta-h_x-\delta(h-Y)\right]+\tau_{xz}\Big|_{z=h}-\tau_{xz}\Big|_{z=Y}. \tag{77}$$

Using the kinematic condition for w at $z=h$ and applying $\tau_{xz}=0$ at $z=h$, $u=0$ at $z=Y$, and $\tau_{xz}\big|_{z=Y}=\mu_1\rho gD\cos\theta$ where $D=h-Y$ is the depth of the layer, yields the depth-averaged momentum equation

$$\frac{\partial}{\partial t}\int_Y^h u\,\mathrm{d}z+\frac{\partial}{\partial x}\int_Y^h u^2\,\mathrm{d}z=gD\cos\theta\left(-\frac{\partial h}{\partial x}+\tan\theta-\delta D-\mu_1\right), \tag{78}$$

At this stage we need to assume a form for the velocity profile $u(z)$ in order to proceed. We derive our velocity profile from the Thin, Shallow, Slippy model, which is undoubtedly a crude approximation, but perhaps slightly less crude than assuming either a constant or a linear velocity profile. In this model we find a relation for the gradient $\partial u/\partial z$,

$$\frac{\partial u}{\partial z}=\frac{\delta I_0\sqrt{g\cos\theta}}{d\Delta\mu}\left[\frac{\sqrt{h-z}(z-Y)}{1-\frac{\delta}{\Delta\mu}(z-Y)}\right]. \tag{79}$$

The "low flux" assumption, or the assumption that Ω (and therefore $Q=\frac{1}{2}\Omega R^2$) is small is equivalent to assuming that the depth of the layer is small, and therefore $z-Y\ll 1$. If we assume this we find a simpler relation for $\partial u/\partial z$,

$$\frac{\partial u}{\partial z}=\frac{\delta I_0\sqrt{g\cos\theta}}{d\Delta\mu}\sqrt{h-z}(z-Y), \tag{80}$$

from which we can obtain a well-behaved velocity profile $u(z)$,

$$u(z)=\frac{\delta I_0\sqrt{g\cos\theta}}{d\Delta\mu}\left\{\frac{4}{15}\left[(h-Y)^{5/2}-(h-z)^{5/2}\right]-\frac{2}{3}(z-Y)(h-z)^{3/2}\right\}, \tag{81}$$

which, upon integration, yields a unique relation between the average velocity U and the depth of the layer D,

$$\int_Y^h u\,\mathrm{d}z=\frac{4}{35}\frac{\delta I_0\sqrt{g\cos\theta}}{d\Delta\mu}D^{7/2}\implies U=\frac{1}{D}\int_Y^h u\,\mathrm{d}z=\frac{4}{35}\frac{\delta I_0\sqrt{g\cos\theta}}{d\Delta\mu}D^{5/2}. \tag{82}$$

We also have

$$\int_Y^h u^2\,\mathrm{d}z=\frac{11}{525}\left(\frac{\delta I_0\sqrt{g\cos\theta}}{d\Delta\mu}\right)^2D^6. \tag{83}$$

Inserting this into the depth-average x-momentum equation yields

$$\frac{\partial U}{\partial t} + \frac{11}{4} U \frac{\partial U}{\partial x} = \frac{5}{7} g \cos\theta \left(-\frac{\partial h}{\partial x} + \tan\theta - \delta \left(\frac{35 d \Delta\mu}{4\delta I_0 \sqrt{g \cos\theta}} \right)^{2/5} U^{2/5} - \mu_1 \right), \tag{84}$$

which forms a system of equations with the depth-average continuity equation, which, recognizing the flux as $Q = UD$, is

$$\frac{\partial h}{\partial t} + \frac{7}{5} \left(\frac{35 d \Delta\mu}{4\delta I_0 \sqrt{g \cos\theta}} \right)^{2/5} U^{2/5} \frac{\partial U}{\partial x} = -\Omega x. \tag{85}$$

4.3.1 Modeling the avalanching regime

While the crude depth-averaged model includes inertia and can accommodate unsteady solutions, it contains no ingredients which can predict the critical angle θ_{start} at which avalanches start. Because of this the model is not fully predictive and θ_{start} is a parameter (depending in general on drum width, drum radius, and granular material) which we must measure in a rotating drum experiment. To capture the full dynamics of the episodic avalanching regime, we insert a condition into our model which specifies that if the total flow across the layer is 0 (the grain pile is at rest) then it cannot flow again until solid body rotation causes the pile angle to reach θ_{start}. At this point the flow is released, which develops into an avalanche. If the rotation rate is slow enough, the avalanche then proceeds until the depth of the layer shrinks to zero first at the toe of the avalanche, and then propagating upwards to the front. The minimum angle of the pile which is achieved when there is no flow corresponds to θ_{stop}. A series of images depicting an avalanche are shown in Figure 8.

5 Comparison with experiment

5.1 Continuous flow and "thin, shallow, slippy"

The thin shallow slippy model yields a prediction for the free surface $h(x)$, and therefore for the average inclination of the flowing layer $\langle\theta\rangle$. Further, the form of the predicted flux Q,

$$Q = \frac{2 I_0 \sqrt{g \cos\theta}}{d} \left(\frac{\Delta\mu}{\delta} \right)^{5/2} q \left(\frac{\tan\theta - \mu_1 - h_x}{\Delta\mu} \right), \tag{86}$$

implies that scaling Q with $W^{5/2}$ eliminates the drum width from the problem (recall $\delta = \mu_{\text{wall}}/W$). To test this prediction of the model we plot of the average angle of the flowing layer $\langle\theta\rangle$ against the $Q/W^{5/2}$ in Figure 9. We observe what appears to be a collapse of the data for widths narrower than $W = 56$ mm. Further, the prediction of the TSS model corresponds well to a portion of the experimental data with the material parameters $\theta_1 = \tan^{-1}\mu_1 = 24.5°$, $\theta_2 = \tan^{-1}\mu_2 = 40°$, and $\mu_{\text{wall}} = 0.38\mu_1$. In this case, we have used the material parameters like fitting parameters and chosen those which best fit the experimental data. It is important to note, however, that the material parameters can and should be measured independent from the drum experiments; further it is only with such measurements that we can make a rigorous test of the fidelity of the model.

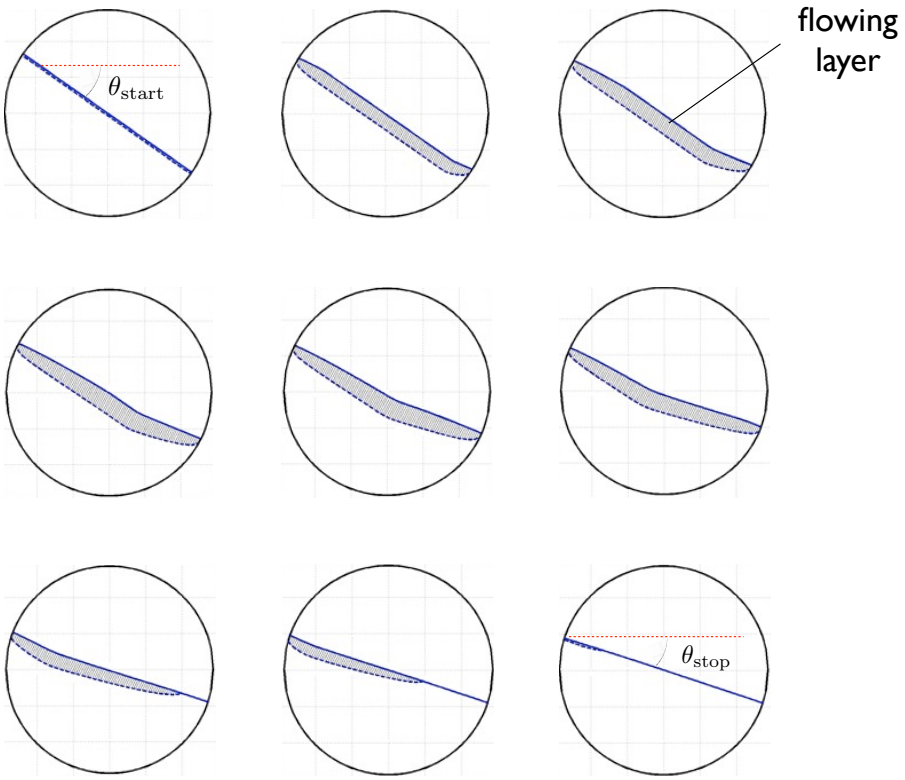

Figure 8: Series of images of a model avalanche calculated using the crude depth-averaged model.

The experimental data differs from the scaling $Q/W^{5/2}$ and the prediction of the model at the upper and lower limits of flow rates explored in the experiment. In both limits the slope of the flowing layer is greater than predicted. At high flow rates, a possible explanation for the discrepancy is the effect of inertia, which should become more important at high flow rates. At the lower flow rates plotted in Figure 9 the system is approaching the transition to episodic avalanching. The failure of the model here may be linked to the transition, which the model does not describe. Finally, for the wide drums $W = 110\,\text{mm}$ and $W = 205\,\text{mm}$, we see that the scaling predicted by the model is no longer valid. This may be due to the fact that the model assumes that W/H is small that the velocity u is uniform across the drum.

Further, the TSS model fails to predict the transition to episodic avalanching. Indeed, the TSS model predicts some pile angle for arbitrarily small flow rates. Of course for a low enough flow rate the predicted thickness of the flowing layer will be smaller than a single particle diameter and the continuum approximation cannot possibly be valid. It is unclear whether it is critical to understand the failure of the continuum assumption and finite size effects in order to predict transition, or if other factors which the model neglects are becoming important.

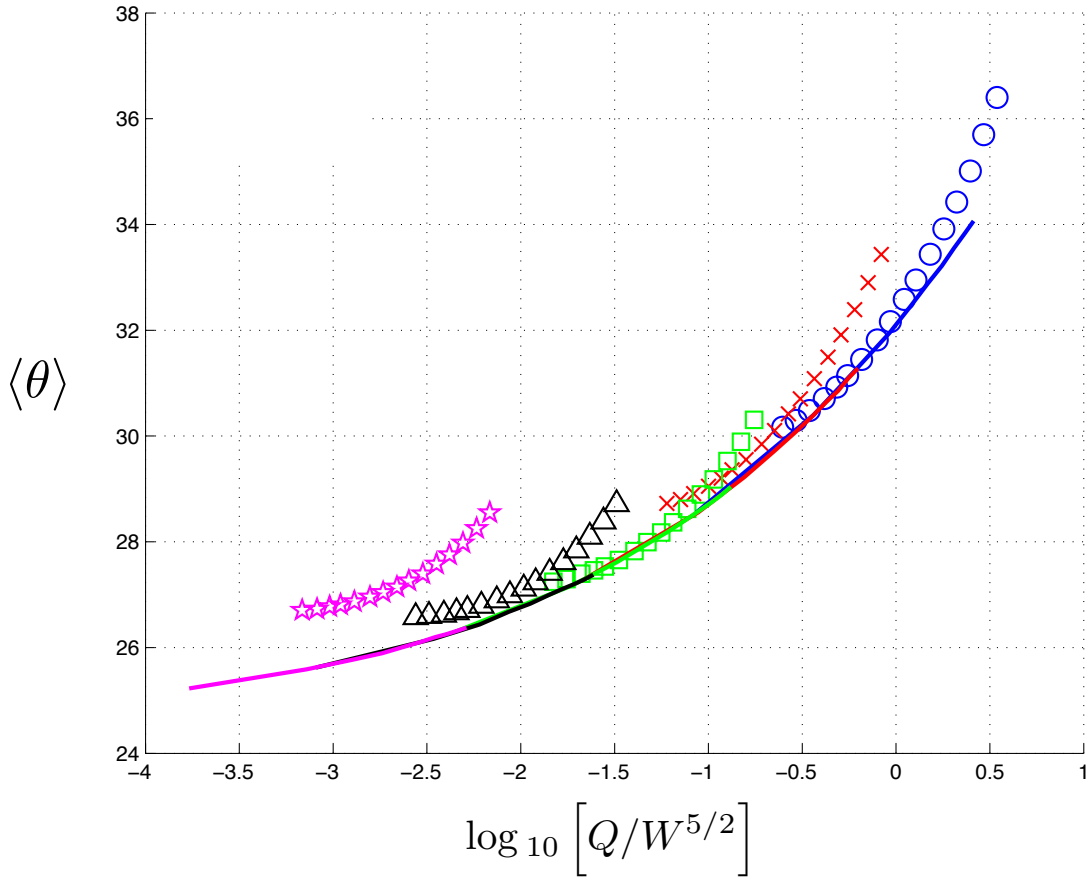

Figure 9: Angle of the flowing layer versus $Q/W^{5/2}$ for five different widths in the Vancouver drum with 3mm diameter glass spheres. Results are shown only for the continuous regime as determined by the minimum value for $\theta_{\max}$. Experimental results: ($\bigcirc$, blue) $W = 17$ mm, ($\times$, red) $W = 31$ mm, ($\square$, green) $W = 56$ mm, ($\triangle$, black) $W = 110$ mm, ($\star$, magenta) $W = 205$ mm. The line is the prediction of the "thin, shallow, slippy" theory the material constants $\theta_1 = \tan^{-1}\mu_1 = 24.5°$, $\theta_2 = \tan^{-1}\mu_2 = 40°$, $\mu_{\text{wall}} = 0.38\mu_1$.

5.2 Episodic avalanching and the crude inertial model

The "thin, shallow, slippy" model is inadequate for modeling the avalanching regime of flow in a rotating drum because it neglects inertial terms in the x-momentum equation. The crude inertial model appears to have the capacity to model an avalanche, but we have not yet had the chance to compare the predicted avalanches with observations. Because it seems plausible that the transition from avalanching to continuous flow with increasing flow rate is linked to the comparative magnitude of the rotation time scale and the avalanche duration, it may be especially important to predict the avalanche duration properly.

Nevertheless, avalanches in the crude inertial model seem reasonable at first glance: the duration is on the order of 0.5 to 1 second, and the halting of the avalanche resembles a wave which begins at the foot of the avalanche and propagates upstream. In addition to this, the model predicts a critical flow rate at which an persistent avalanching solution no longer exists. This transition depends on our model choice of θ_{start} and occurs because the rotation of the drum is fast enough (and the avalanche duration long enough) such that the flow incurred in the avalanche never decreases all the way to zero. Figure 10 shows a plot of θ versus Q and a phase space plot in $\{\dot{\theta}, \theta\}$-space for the crude inertial model. In the plot of θ versus Q, a transition from episodic avalanching to continuous flow is predicted around $Q \approx 300\,\text{mm}^2/\text{sec}$. The plot in $\{\dot{\theta}, \theta\}$-space shows two phase space trajectories. The blue solid line plots a trajectory taken by the system in in its episodic avalanching state and the red dotted line plots a trajectory taken by the system for a higher flow rate at which the system reaches the continuous flow state even when an avalanche is initiated at θ_{start}. We see in the trajectory taken by the system with a higher flow rate that the rate of change of the pile angle, which is analogous to the inertia contained in the avalanche, is diminished. Further, the minimum pile angle achieved on the trajectory for the higher flow rate is not quite as low as the minimum pile angle achieved for the system with a smaller flow rate. In the trajectory shown here, the system nearly reaches the cessation of flow as the rate of change of the pile angle approaches its value for solid body rotation, but subsequently drifts into the continuous flow solution.

6 Discussion

With the results of the two models in hand we can begin to sketch out a global understanding of the system. We see first of all that the thin, shallow, slippy model appears to accurately describe the dependence of the pile slope on flow rate for a certain range of flow rates. This lends confidence to the validity of $\mu(I)$ frictional rheology. At high flow rates, the thin shallow slippy model fails, but this is likely because of the importance of inertial terms and not a failure of the $\mu(I)$ law. Near the transition to episodic avalanching, however, it appears that the thin, shallow, slippy model begins to slightly underestimate the angle of the pile. We can only speculate to the reason for this discrepancy, but it seems possible that it is linked to the same physics that leads eventually to the disappearance of the continuous flow regime. One possible explanation for this discrepancy (and perhaps the transition as well [8]) is the finite thickness of the flowing layer.

Secondly, while the crudity and incompleteness of the crude inertial model mean it cannot be used as a quantitative and predictive model, it provides some basis for the notion

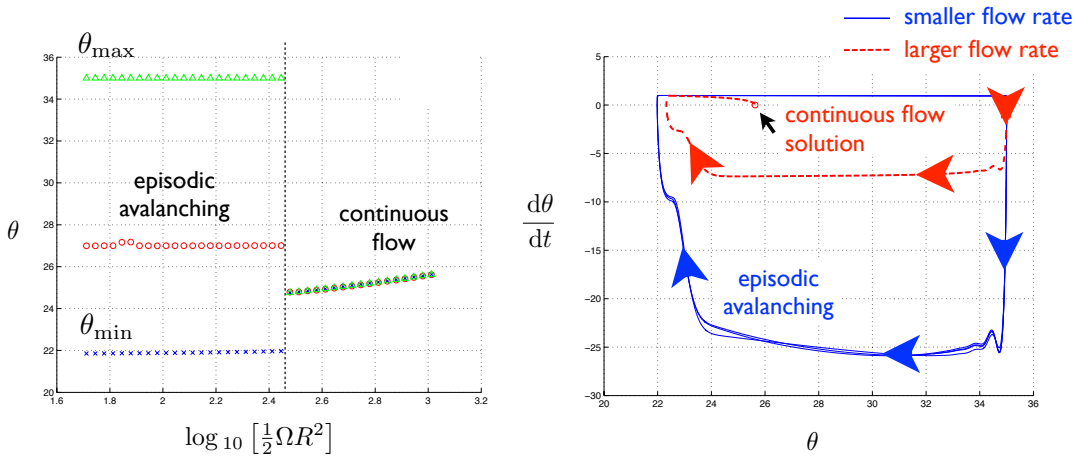

Figure 10: A θ versus Q plot (left) and a phase space plot (right) for the crude inertial model. (Left) a θ versus Q plot as predicted by the crude inertial model with $\theta_{\text{start}} = 35°$. Episodic avalanching cannot be observed as a steady solution in the model after $Q \approx 300\ \text{mm}^2/\text{sec}$. (Right) a plot showing transient phase space trajectories of episodic avalanching and continuous flow solutions in $\{\dot{\theta}, \theta\}$-space. When episodic avalanching is observed we see that $\dot{\theta}$ and the inertia of the avalanche are large enough to bring the avalanching to a small value of θ at which the flow stops completely. At larger flow rates, the $\dot{\theta}$ and the inertia of the avalanche are insufficient to bring the pile angle low enough to halt the avalanche.

that an increase in rotation rate can decrease the grain inertia which builds during an avalanche. This is important because the inertia contained in the avalanche controls the amount of material it moves; and the more material which is moved, the more the angle of the pile is decreased. Finally, the pile angle must decrease sufficiently for the flow to cease completely. If too little material is carried by the avalanche, the pile angle will remain high enough to continue driving flow, and the system will undergo damped oscillations in flow rate until settling into a continuous flow state. This implies that there is some critical flow rate which diminishes avalanche inertia enough such that the episodic avalanching solution no longer exists.

A sketch of our current understanding of the system — the "big picture" — is shown in Figure 11. At low flow rates, $Q < Q_1$, only episodic avalanching is observed. Below this critical flow rate, the continuous flow solution cannot exist in steady-state; this perhaps can be linked to a minimum thickness for the flowing layer, or an increase in effective friction for layers on the order of a particle diameter. At intermediate flow rates, $Q_1 < Q < Q_2$, both the episodic avalanching regime and the continuous flow solution are observed. At high flow rates, $Q > Q_2$ only continuous flow is observed. The episodic regime can no longer exist in steady-state because the rotation of the drum prevents any avalanche from building up enough inertia to cause cessation of flow.

Further, we can speculate as to why hysteresis is observed in sand where intermittency is observed with spherical glass beads. It may be true that for any granular material there are stochastic fluctuations in the volume fraction of the flow (affecting the effective internal

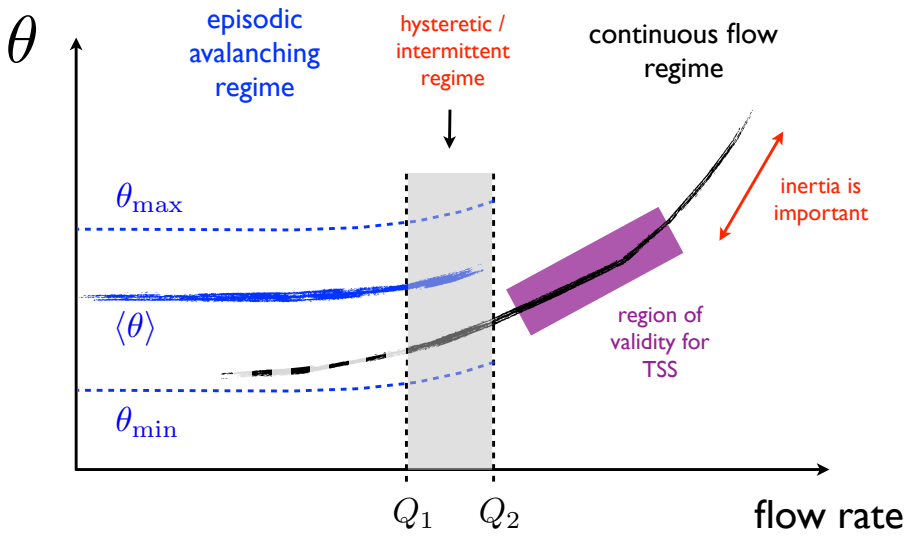

Figure 11: The big picture: a sketch of our current understanding

friction coefficient), velocity profile, and pressure forces. These stochastic fluctuations could imply that the critical flow rates Q_1 and Q_2 fluctuate as well, which could result in intermittent transition between regimes at intermediate flow rates. In this theory, stochasticity would still be present for sand but would be relatively small compared to other forcings in the system. An explanation for the relative unimportance of stochasticity is perhaps related to the larger effective friction coefficient observed with sand.

Much work remains. For the thin, shallow, slippy model, it should be verified that discrepancies at high flow rates are due to inertia. This could be done preliminarily by including the effects of inertia as a correction to the $\mathrm{Fr} = 0$ solution. An asymptotic expansion can only be extended so far, however, as it is still unable to accommodate flow rates which result in pile angles $\theta > \theta_2$, as the leading order inertialess solution no longer exists in this case. Accommodating higher flow rates than this would likely require two-dimensional simulations.

Further, the initial aim of this work was to describe the transition from continuous flow to episodic avalanching, a goal which remains unfulfilled. Now that it is known that the $\mu(I)$ frictional rheology is inadequate by itself to predict this transition (as well as underpredicting the angle of the flowing layer close to transition), some creativity is necessary to proceed. Perhaps most promising approach would be to consider effects of the finite thickness of the flowing layer depth and the failure of the continuum approximation. This may prove difficult, as connecting microscopic physics to the observed macroscopic behavior of granular flows is a long-standing problem. Discrete element numerical simulations may aid greatly in this pursuit.

For the crude avalanching model, it must first of all be confirmed that the avalanche dynamics are captured correctly. If the dynamics are incorrect, the model must be refined. Capturing avalanches correctly may require two-dimensional simulations. The proposed hypothesis for the transition from episodic avalanching to continuous flow is that increasing

flow rates limit the build up of inertia in the avalanche, which in turn limits the change in pile angle. An accurate model for avalanching could explore this hypothesis fully. Finally, it would be desirable to be able to predict the width-dependent θ_{start}, the angle at which avalanches are initiated. With a method to predict θ_{start}, and accurate avalanching model could potentially be fully predictive and dependent only on independently measured material parameters.

7 Acknowledgements

I would like to extend a hearty thanks to the directors Stefan Llewellyn Smith, Claudia Cenedese, and Eric Chassignet, the principle lecturer Paul Linden, and staff of the 2013 WHOI program in Geophysical Fluid Dynamics. It was an unforgettable summer. I would like to thank Neil Balmforth for proposing the project and yielding a great deal of time to work closely with me, perform experiments over the summer and for contributing results from his lab in Vancouver. I would like to thank Anders Jensen for helping to set-up the rotating drum in Woods Hole and tolerating the peculiarities of experiments with granular materials and glass beads with low interparticle friction coefficients. Finally, it is with great understatement that I thank the other Fellows of the program, whose friendship was forged through trials of both mind and matter, in the sublime highs and devastating lows of WHOI softball, and the blackboard-lined crucible of Walsh Cottage.

A Data for 2 mm and 1.5 mm glass beads

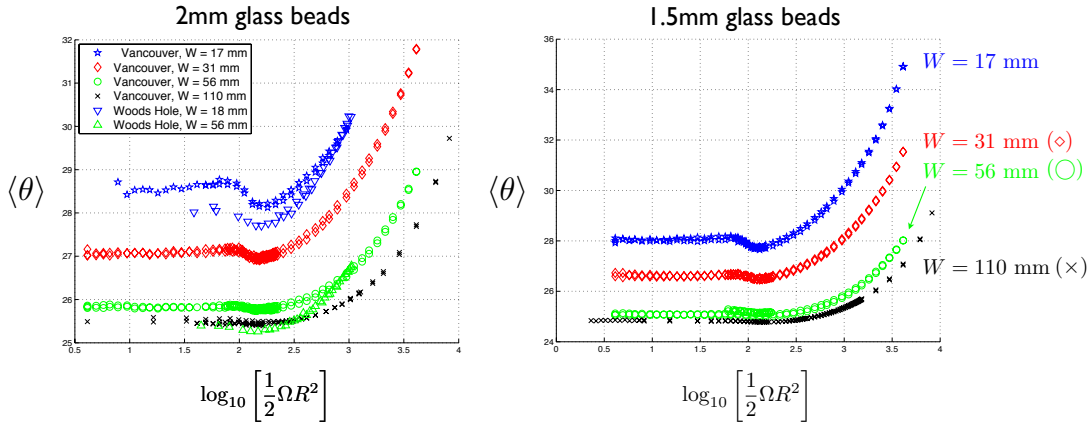

Figure 12: (Left) θ versus Q for 2 mm from experiments in Vancouver and Woods Hole. The Woods Hole results do not line up as well with the Vancouver results as for the 3 mm glass beads. This may have to do with errors associated with the alignment of the Woods Hole camera. It also appears that θ is increasing much faster with Q for both $W = 17$ mm ($W = 18$ mm for Woods Hole) and $W = 56$ mm. The cause of this is unknown. (Right) θ versus Q for the 1.5 mm glass beads from experiments in Vancouver.

References

[1] M Caponeri, S Douady, S Fauve, and C Laroche, *Dynamics of avalanches in a rotating cylinder*, Mobile Particulate Systems, (1995), pp. 331–366.

[2] Alain de Ryck and Olivier Louisnard, *Depth and minimal slope for surface flows of cohesive granular materials on inclined channels*, Journal of Fluid Mechanics, 727 (2013), pp. 191–235.

[3] Raphaël Fischer, Philippe Gondret, Bernard Perrin, and Marc Rabaud, *Dynamics of dry granular avalanches*, Phys. Rev. E, 78 (2008), pp. 1–4.

[4] Raphaël Fischer, Philippe Gondret, and Marc Rabaud, *Transition by intermittency in granular matter: From discontinuous avalanches to continuous flow*, Phys. Rev. Lett., 103 (2009), pp. 1–4.

[5] Yoël Forterre and Olivier Pouliquen, *Flows of dense granular media*, Annu. Rev. Fluid Mech., 40 (2008), pp. 1–24.

[6] Isaac Goldhirsch, *Rapid granular flows*, Annual Review of Fluid Mechanics, 35 (2003), pp. 267–293.

[7] Nitin Jain, J M Ottino, and R M Lueptow, *An experimental study of the flowing granular layer in a rotating tumbler*, Physics of Fluids, 14 (2002), pp. 1–12.

[8] Pierre Jop, Yoël Forterre, and Olivier Pouliquen, *Crucial role of sidewalls in granular surface flows: consequences for the rheology*, J. Fluid Mech., 541 (2005), p. 167.

[9] ——, *A constitutive law for dense granular flows*, Nature, 441 (2006), pp. 727–730.

[10] GFD MiDi, *On dense granular flows*, Eur. Phys. J. E, 14 (2004), pp. 341–365.

[11] D J Parker, A E Dijkstra, T W Martin, and J P K Seville, *Positron emission particle tracking studies of spherical particle motion in rotating drums*, Chemical Engineering Science, 52 (1997), pp. 2011–2022.

[12] Sylvain Courrech Du Pont, Raphaël Fischer, Philippe Gondret, Bernard Perrin, and Marc Rabaud, *Instantaneous velocity profiles during granular avalanches*, Phys. Rev. Lett., 94 (2005), pp. 1–4.

[13] Patrick Richard, Mario Nicodemi, Renaud Delannay, Philippe Ribière, and Daniel Bideau, *Slow relaxation and compaction of granular systems*, Nat Mater, 4 (2005), pp. 121–128.

[14] Jean-Noel Roux and Gael Comb, *Quasistatic rheology and the origins of strain*, Physics of Granular Media, 3 (2002), pp. 131–140.

[15] Nicolas Taberlet, Patrick Richard, and E John Hinch, *S shape of a granular pile in a rotating drum*, Phys. Rev. E, 73 (2006), pp. 1–4.

[16] K Yamane, M Nakagawa, S A Altobelli, T Tanaka, and Y Tsuji, *Steady particulate flows in a horizontal rotating cylinder*, Physics of Fluids, 10 (1998), pp. 1419–1427.

[17] R Y Yang, R P Zou, and A B Yu, *Microdynamic analysis of particle flow in a horizontal rotating drum*, Powder Technology, 130 (2003), pp. 138–146.